This is a preprint of a published paper, in "Composite Structures" by Elsevier availabe at https://doi.org/10.1016/j.compstruct.2019.111435

On the damage mechanism of high-speed ballast impact and compression after impact for CFRP laminates

Yuliang Hou[a,b,*], Ying Tie[a], Cheng Li[a], Liang Meng[c,*], Thaneshan Sapanathan[b,d], Mohamed Rachik[b]

[a]*School of Mechanical Engineering, Zhengzhou University, Science Road 100, 450001, Zhengzhou, China*
[b]*Laboratoire Roberval, FRE UTC-CNRS 2012, Sorbonne universités, Université de Technologie de Compiègne, Centre de recherche Royallieu, CS60319, 60203, Compiègne Cedex, France*
[c]*State IJR Center of Aerospace Design and Additive Manufacturing, Northwestern Polytechnical University, 710072 Xian, China*
[d]*Institute of Mechanics, Materials and Civil Engineering, UCLouvain, B-1348 Louvain-la-Neuve, Belgium*

Abstract

Single and multiple track-ballast impacts are investigated for the CFRP laminates used in train carbodies. Numerical simulations have been performed to study the damage behaviors of CFRP laminates during ballast impacts and compressions after ballast impact (CABI). Intralaminar and interlaminar damages are successfully predicted using continuum damage mechanics and cohesive zone model, respectively. It reveals that, for a high-speed ballast impact, delamination occurs during the damage initiation and appears at several interfaces nearby the impacted side of the specimen. After that, fiber breakage and matrix cracking appear, while delamination continuously extends until the failure. Repeated ballast impacts on the same site and different sites of specimens show significant increase of delamination while indicating less intralaminar damage. Furthermore, CABI simulations show that, the residual compression strength decreases in a nonlinear manner with the increase of impact energy. To bear the same impact energy, less detrimental effect is caused when one impact is replaced by two or more impacts.

Keywords: High-speed train, CFRP laminates, Ballast impact, Compression after ballast impact, Impact damage

1. Introduction

Composite materials, especially carbon fiber reinforced polymer (CFRP) laminates, have been widely used in the design and manufacturing of high-speed train carbodies due to their high specific stiffness and strength [1–5]. CFRP laminates provide excellent fuel efficiency and fatigue resistance. However, they are prone to damages caused by impact issues, which significantly reduce the residual compressive strength and impact-resistance [6–12]. Moreover, ballast impacts

*Corresponding author.
Email addresses: yulianghou@zzu.edu.cn (Yuliang Hou), liang.meng@nwpu.edu.cn (Liang Meng)

are frequently encountered by train carbodies, and this type of impacts cannot be avoided during the service of high-speed trains [13–15]. Since the damage within the composites caused by impact is complex, it is challenging to evaluate the residual compressive strength and impact-resistance of CFRP laminates after ballast impacts. Hence, more investigations are required to comprehensively understand the damage mechanisms due to ballast impact and damage evaluation during the compression test after impact.

Recently, numerous experimental and numerical studies have been performed for composite skins and panels to understand the impact behaviors [16–24]. Ansari et al. [20] investigated the low- and high-velocity impact behaviors of fiber reinforced polymer (FRP) laminates using numerical simulations. In the low-velocity impact case, the delamination initiated from the mid thickness of the FRP laminates, but its size was relatively limited. While, the impactor with high velocity caused delamination starting from the mid thickness and propagating towards the back face of the FRP laminates. Li et al. [23] sysmetically evaluated the predictive capability of various damage criteria for CFRP laminates under low-velocity impact. The Hashin damage criteria were recommended to predict intralaminar damages of composite laminates for a low-velocity impact simulations in comparison with the maximum stress and Tsai-Wu damage criteria [23]. Following a low-velocity impact, compression after impact (CAI) test is frequently carried out to identify the residual compressive strength and damage evaluation within CFRP laminates [25–33]. However, it is extremely difficult in CAI simulation to predict the damage growth during compression with reliable accuracy.

In the work of Ghelli et al. [26], drop-weight impact and CAI tests were performed on carbon/epoxy laminates with different thicknesses, according to ASTM standards. The laminates possessing relatively small thicknesses exhibited elastic instability during CAI tests, regardless of the overall dimensions and fiber orientations. And thus, this affected the measurement of residual compressive strength of the impacted specimens. Hence, in the case of smaller specimens, compressive failure mainly occurs at the impact-damaged zone, while the residual compression strength is significantly reduced by the preexisting delamination area. Short et al. [25] experimentally studied the effect of delamination on compressive failure and damage growth by introducing an artificial delamination geometry consisting of Polytetrafluoroethylene (PTFE) film between composite layers. It was found that the delamination size and through-thickness position directly affect the compressive strength of the composites [25]. The failure load decreases with the increase of delamination size and the decrease of the through-thickness position of the delamination. A meso-scale finite element (FE) model was developed by Zhao et al. [31] to identify the damage mechanism of a triaxially braided CFRP laminates under compressive loads. Based on the meso-scale model, free-edge effect was identified to appear along the free edges of composite laminates under transverse compressive loads, which finally caused a premature edge-initiated interface failure.

To accurately capture the damage behaviors of CFRP laminates, numerical models using continuum damage mechanics (CDM) has also been exploited to simulate the fiber breakage and matrix cracking (intralaminar damages), while cohesive zone model (CZM) has been used to simulate the delamination (interlaminar damage) [7, 34]. In the work of Tan et al. [35], the aforementioned simulation strategy was used to model intra- and inter-laminar damages of CFRP laminates T700/M21 during low-velocity impact and CAI tests. Their study successfully predicted the damage distributions and energy dissipation corresponding to each damage mode. It indicates that the method has the capability to effectively capture both intralaminar and interlaminar damages for a range of impact energies, as well as the complex damage origins and residual compressive strength after impact [35].

Table 1: Dimension range of ballast stones used in rail tracks in different European countries [36]. (Unit: mm)

Country	Dimension (min/max)
France	25/50
Germany	22.5/63
Italy	30/60
Spain	32/63
Belgium	25/50

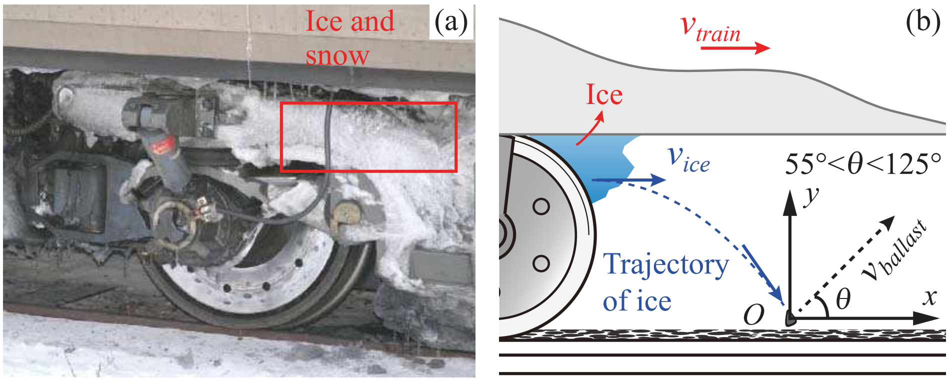

Figure 1: Illustration of (a) snow and ice formed under train carbody and (b) ballast impact caused by the ice fall [37].

The existing studies of low-velocity impact and CAI tests for composite materials consider the impactors with hemisphere or sphere shapes to perform impacts. These studies do not represent the realistic nature of the ballast impact for the following reasons. Commonly, the average mass of the ballast stone is 0.06 kg, and the principal dimension varies within a range for various European countries [36], as listed in Table 1. The presence of sharp corners and edges usually found in the ballast stones, increases the likelihood of impact damage on the train structures. Besides, very few studies are available on simulation of ballast impact and compression after ballast impact (CABI) tests. However, according to the work of Nistor [37], the causes of ballast impacts are diverse: the sudden change of train speed, the vibrations induced by the rolling stocks, etc. Another common origin of such impact found in literature is due to snowfall or ice, which accumulated under the train cargo during locomotion. The deposited ice formed beneath the train cargo, becomes heavier over time and falls on the ballast tracks leading to the detachment of ballast stones. Some ballast stones can reach sufficiently high to damage the train carbody [38], as demonstrated in Fig. 1. The ballast projects with an angle (θ in Fig. 1b), and its critical range to cause an impact on the train carbody varies from 55° to 125° [37]. In other words, if the value of θ is greater than 55° and smaller than 125°, the bouncing ballast stones probably impact the train carbody. Moreover, due to the dynamic nature of the ballast impact along with the train speed, an instantaneous angle, different from θ will become the onset of impact angle. Here, a stationary composite plate is modeled for the normal ballast impact ($\theta = \pi/2$). That is, a normal impact with the non-zero friction (the friction coefficient is 0.3) is considered to investigate the damage behaviors of the CFRP laminates during single and multiple ballast impacts.

During the ballast impact on train carbody [37], the relative velocity between the ballast stone and the train reaches in the range of [33.33, 61.11] (unit: m/s). The impact velocity is significantly higher than that assigned during low-velocity impact test. This dissimilarity is crucial and it significantly affects the damage behaviors in both the ballast impact and CABI tests compared to low-velocity impact tests. However, recent studies on high-speed impact [17, 24, 27] provided the final damaged specimens, and the post-treatment of these samples with only limited information. Therefore, numerical investigation has been performed in this study to better understand the fundamental damage mechanism of high-speed ballast impact for CFRP laminates. It can provide vital insights for the impact-resistance assessment during the design stage of high-speed train carbodies.

2. Composite damage models

The failure modes in laminated composites are commonly classified into intralaminar and interlaminar damages, in which the intralaminar damage is characterized by fiber breakage and matrix cracking, while the interlaminar damage mainly presents delamination.

2.1. Intralaminar damage

Hashin damage criteria [39] considering four damage modes: tensile and compressive damages of both fiber and matrix, which have been used to predict the intralaminar damage initiation of CFRP laminates. Besides, residual strength of damaged laminates is computed using damage evolution, which is based on the specification of fracture energy corresponding to those four damage origins. The corresponding damage evolution using CDM is adopted after the first appearance of intralaminar damage [34].

With respect to those four failure modes, each is taken into account using the component of the stress tensor associated with the damage plane described by quadratic equations [40], given in Eqs. (1-4).

Fiber tensile damage ($\sigma_{11} \geq 0$):

$$(\frac{\sigma_{11}}{X_t})^2 + \alpha(\frac{\sigma_{12}}{S_L})^2 \geq 1 \tag{1}$$

Fiber compressive damage ($\sigma_{11} \leq 0$):

$$(\frac{\sigma_{11}}{X_c})^2 \geq 1 \tag{2}$$

Matrix tensile damage ($\sigma_{22} \geq 0$):

$$(\frac{\sigma_{22}}{Y_t})^2 + (\frac{\sigma_{12}}{S_L})^2 \geq 1 \tag{3}$$

Matrix compressive damage ($\sigma_{22} \leq 0$):

$$(\frac{\sigma_{22}}{2S_T})^2 + [(\frac{Y_c}{2S_T})^2 - 1](\frac{\sigma_{22}}{Y_c})^2 + (\frac{\sigma_{12}}{S_L}) \geq 1 \tag{4}$$

where σ_{11}, σ_{22} and σ_{12} are the components of stress tensor, α is a coefficient denoting the shear stress contribution to the fiber tensile damage, and it varies in the range of [0, 1]. In this study, the value of $\alpha = 1$ is used. Moreover, other strength terms $X_{t,c}$, $Y_{t,c}$, $S_{L,T}$ of the CFRP laminates are listed in Table 2.

Once intralaminar damage in CFRP laminates is identified using the damage criteria expressed in Eqs. (1-4), the stiffness matrix $\boldsymbol{C}$ corresponding to the finite element (FE) stress-strain equilibrium is updated at that particular analysis increment. Subsequently, the constitutive relation of CFRP laminates is degraded by a material property degradation model (MDM) after the detection of damaged elements obeying any of those four possible damage origins. A damage evolution law base on CDM in Abaqus/Explicit [41], is used to determine the material property degradation in each damage mode. When the damage appears in CFRP laminates, the constitutive relation is defined by:

$$\boldsymbol{\sigma} = \begin{bmatrix} \sigma_{11} \\ \sigma_{22} \\ \sigma_{12} \end{bmatrix} = \boldsymbol{C}_d \boldsymbol{\varepsilon} = \frac{1}{D_f} \begin{bmatrix} (1-d_f)E_1 & (1-d_f)(1-d_m)\upsilon_{21}E_1 & 0 \\ (1-d_f)(1-d_m)\upsilon_{12}E_2 & (1-d_m)E_2 & 0 \\ 0 & 0 & (1-d_s)G_{12}D_f \end{bmatrix} \begin{bmatrix} \varepsilon_{11} \\ \varepsilon_{22} \\ \varepsilon_{12} \end{bmatrix} \tag{5}$$

where $\boldsymbol{\sigma}$ and $\boldsymbol{\varepsilon}$ denote stress and strain tensors, respectively. E_1 and E_2 represent Young's modulus in the x and y directions, G_{12} represents the shear modulus, υ_{12} and υ_{21} refer to Poisson's ratios in respective shear directions. $\boldsymbol{C}_d$ is the degraded stiffness matrix, and D_f is the damage indicator, which varies from 0 to 1 corresponding to the pristine and damaged material states, respectively. Moreover, D_f is defined by:

$$D_f = 1 - (1-d_f)(1-d_m)\upsilon_{12}\upsilon_{21} \tag{6}$$

where d_f, d_m and d_s are the damage variables corresponding to fiber, matrix and shear damage modes, respectively. They are computed using damage variables d_f^t, d_f^c, d_m^t and d_m^c, which are respectively associated with those four failure modes, and given by:

$$d_f = \begin{cases} d_f^t & \text{if } \sigma_{11} \geq 0 \\ d_f^c & \text{if } \sigma_{11} < 0 \end{cases} \tag{7}$$

$$d_m = \begin{cases} d_m^t & \text{if } \sigma_{22} \geq 0 \\ d_m^c & \text{if } \sigma_{22} < 0 \end{cases} \tag{8}$$

$$d_s = 1 - (1-d_f^t)(1-d_f^c)(1-d_m^t)(1-d_m^c) \tag{9}$$

After damage initiation, the damage variable of each failure mode is assessed using the criterion of:

$$d = \frac{\delta_{eq}^{f}(\delta_{eq} - \delta_{eq}^{0})}{\delta_{eq}(\delta_{eq}^{f} - \delta_{eq}^{0})} \tag{10}$$

where δ_{eq}^{0} refers to the initial equivalent displacement where the damage starts to grow in a particular failure mode, and δ_{eq}^{f} denotes the final equivalent displacement when the composite ply is fully damaged in the corresponding mode. Wherein, δ_{eq}^{0} is a function of the fracture energy G_C, and δ_{eq}^{f} is dependent on Young's modulus E and maximum allowable strength S, as listed in Table 2. Moreover, δ_{eq} is the equivalent displacement for a given applied strain. To avoid the mesh dependency problem, the computation of the equivalent displacements considering the characteristic finite element length (L_c) is employed in the damage evolution law as a function of stress-displacement rather than a function of stress-strain.

2.2. Interlaminar damage modeling

Cohesive zone model (CZM) obeys a traction-separation law, where the traction stress and separation displacement of the nodes on the interaction surface shared by the adjacent plies [42]. The CZM method is used to describe the interlaminar damage initiation, especially the delamination between different layers within CFRP laminates.

The interaction area of two adjacent layers is considered as matrix materials. Therefore, the interlaminar damage is regarded as a linear elastic behavior before the appearance of delamination. The traction stress tensor $\boldsymbol{t}$ acting on the interaction surface, consisting of a normal traction t_n and two shear tractions, t_s and t_t, is assessed by:

$$\boldsymbol{t} = \begin{bmatrix} t_n \\ t_s \\ t_t \end{bmatrix} = \boldsymbol{C\delta} = \begin{bmatrix} C_n & 0 & 0 \\ 0 & C_s & 0 \\ 0 & 0 & C_t \end{bmatrix} \begin{bmatrix} \delta_n \\ \delta_s \\ \delta_t \end{bmatrix} \tag{11}$$

where $\boldsymbol{C}$ refers to the stiffness matrix whose components are given in Table 2, and $\boldsymbol{\delta}$ represents the separation displacement vector. The subscripts (n, s, t) of interaction stiffness C denote three directions that respectively correspond to the three fracture modes, as shown in Fig. 2.

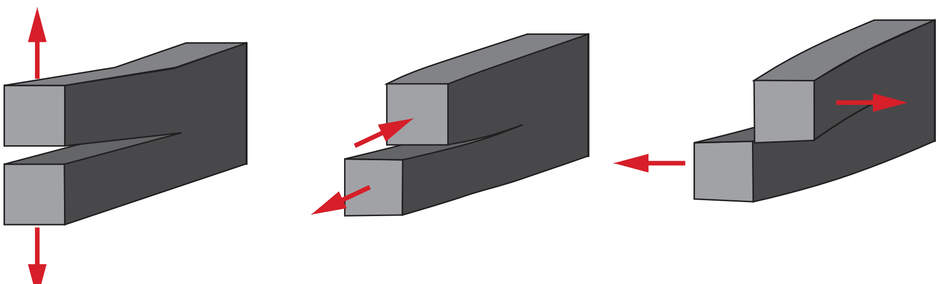

Figure 2: Fracture modes for interlaminar damage: (a) normal tension, (b) in-plane (first) shear and (c) out-of-plane (second) shear.

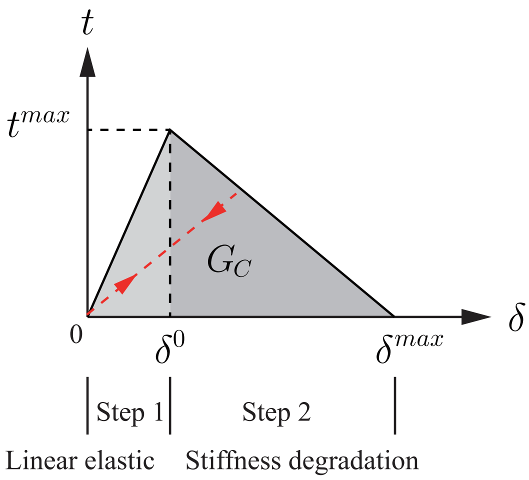

Figure 3: Traction-separation law used for the CZM approach.

The interlaminar damage within the composite laminates is governed by a quadratic separation law. In this law, delamination appears when the quadratic interaction function reaches 1, which is given by:

$$(\frac{t_n}{t_n^{max}})^2 + (\frac{t_s}{t_s^{max}})^2 + (\frac{t_t}{t_t^{max}})^2 \geq 1 \tag{12}$$

where t_n^{max}, t_s^{max} and t_t^{max} are the maximum values of the normal and shear tractions, respectively. Similar to the intralaminar damage, the damage evolution is classified into two steps, as illustrated in Fig. 3. Before the appearance of delamination, the interaction defined by a linear elastic behavior (Step 1 in Fig. 3). Once the damage criterion in Eq. (12) is satisfied, the cohesive stiffness begins to degrade. Abaqus/Explicit [41] allows choosing either a linear or an exponential softening law during the degradation step. In this study, a linear softening behavior has been used to describe the stiffness degradation (Step 2 in Fig. 3).

In Fig. 3, G_C represents the fracture energy released during the delamination under a mix mode of failure. It is formulated according to Benzeggagh-Kenane fracture criterion [43] given by:

$$G_C = G_C^I + (G_C^{II} - G_C^I)(\frac{G_C^{II} + G_C^{III}}{G_C^{II} + G_C^I})^\eta \tag{13}$$

where G_C^I, G_C^{II} and G_C^{III} refer to the critical values of fracture energy required to cause the failure with fracture mode I, II and III, respectively. And, the parameter η denotes a cohesive zone property and its value of 1.45 is used in the simulation [22].

3. Numerical modeling procedure

3.1. Material properties and geometry of laminates

To predict the ballast impact behaviors and compression strength after ballast impact of CFRP laminates, the properties of multidirectional composite panels manufactured using infusion process (by Technalia) are considered in this study. The properties of carbon fibers SIGRAFIL® C30

T050 EPY, manufactured by SGL Group, and the resin Resoltech 1800, are specified to the model. The model uses the same thickness of experimentally observed one after curing (4.8 mm for 16 plies), and the stacking sequence is $[(45/-45/0/90)_2]_S$. Accordingly, the mechanical properties of the composite laminates are described based on the literature [37], and reported in Table 2. Subsequently, the CFRP laminates with the dimension of 150 mm × 100 mm are used, as shown in Fig. 4a.

Table 2: Mechanical properties of the used CFRP laminates (C30 T050 EPY/Resoltech 1800) [37].

Elastic properties		**Damage properties**	
Intralaminar damage modeling			
Young's modulus, E_1 (GPa)	126	Longitudinal tensile strength, X_t (MPa)	1740
Young's modulus, E_2 (GPa)	7.6	Longitudinal compressive strength, X_c (MPa)	757
Shear modulus, G_{12}, G_{13} (GPa)	3.9	Transverse tensile strength, Y_t (MPa)	26
Shear modulus, G_{23} (GPa)	2.3	Transverse compressive strength, Y_c (MPa)	138
Poisson's ratio υ_{12}	0.35	Transverse shear strength, S_T (MPa)	41
		Longitudinal shear strength, S_T (MPa)	25
		Fracture energy fiber tension, G_C^{Xt} (kJ/m^2)	75
		Fracture energy fiber compression, G_C^{Xc} (kJ/m^2)	37.5
		Fracture energy matrix tension, G_C^{Yt} (kJ/m^2)	1
		Fracture energy matrix compression, G_C^{Yt} (kJ/m^2)	12.5
Interlaminar damage modeling			
Interface stiffness, C_n (GPa/mm)	1	Maximum normal traction, t_n^{max} (MPa)	20
Interface stiffness, C_s, C_t (GPa/mm)	2	Maximum shear traction, t_s^{max}, t_t^{max} (MPa)	80
		Critical energy release rate mode I, G_C^I (kJ/m^2)	0.512
		Critical energy release rate mode II, III, G_C^{II}, G_C^{III} (kJ/m^2)	2

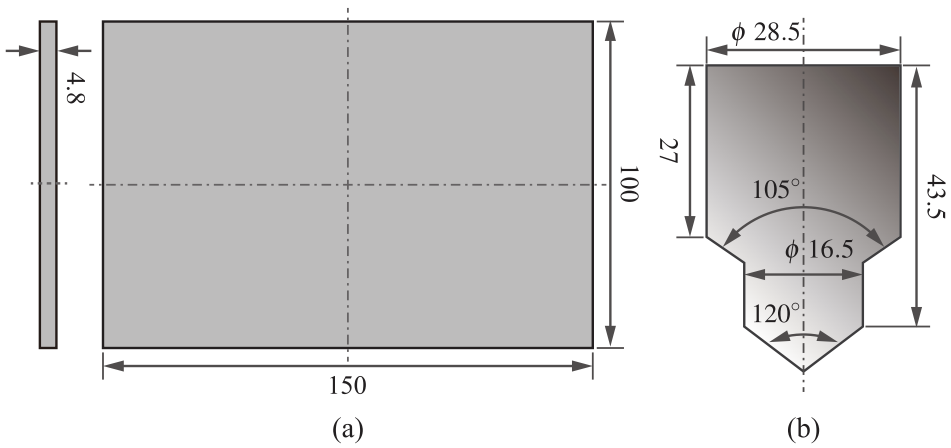

Figure 4: Geometry information of: (a) CFRP laminates and (b) conical impactor used for ballast impact test. (Unit: mm)

3.2. Numerical testing methods

In this study, numerical tests of ballast impact and CABI have been performed to investigate the impact behaviors and residual compression strength after ballast impact of the CFRP laminates.

Thereinto, the numerical ballat impact tests have been carried out according to French standard NF/F07-101 [44]. The model consists of a conical impactor, to well represent the ballast impact on the CFRP laminates of the train carbody to assess its impact behaviors. The geometrical specifications of the impactor are illustrated in Fig. 4b. The mass of the impactor was assigned as 0.06 kg, equal to the average mass of ballast stone used in train tracks. The CFRP laminates were placed on a flat support fixture with a 125 mm × 75 mm rectangular cut-out allowing the impactor to collide the laminates without interference. Moreover, the laminates were fastened using four rubber clamps according to the ASTM D7136/D7136-12 standard [45], to represent the realistic nature of the experiment, as illustrated in Fig. 5a. At the beginning of the ballast impact process, various initial velocities were prescribed to the impactor. Impact responses, including impact force and damage dissipation energy, of CFRP laminates caused by ballast impacts were obtained to study the influence of impact energy on the damage behaviors.

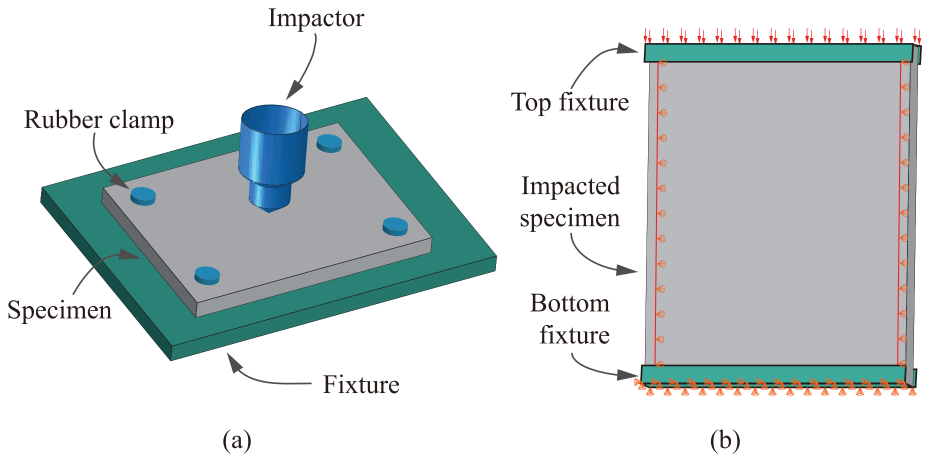

Figure 5: Schematic illustration of the model used for: (a) ballast impact and (b) compression after ballast impact (CABI).

After the ballast impacts, CABI simulations heve been implemented on the impacted specimens accordingly to the ASTM D7137/D7137-12 standard [46]. An appropriate fixture assembly was placed between the laminates and end-loaded under compression, as shown in Fig. 5b. One side of the pre-impacted laminates was fastened using the bottom fixture with all degrees of freedom (DOFs) fixed, and the other side was encased into the top fixture. During the CABI simulation, a compression displacement was prescribed for the top fixture until the pre-impacted laminates completely failed.

3.3. Finite element models

Numerical simulations have been performed to comprehensively understand the damage initiation and growth during ballast impact and CABI processes. To achieve this target, 3D FE model was constructed using Abaqus/Explicit software [41]. Firstly, the numerical simulation of ballast impact was performed using the FE model shown in Fig. 6. To reduce the computational time without compromising on the calculation accuracy, eight-node continuum shell elements with reduced integration (element type: SC8R), were used to mesh each composite layer in the CFRP laminates. The elements of each layer are regular and oriented according to the fiber orientation. Moreover, a set of cohesive elements with zero thickness (element type: COH3D8) were included to describe the interface between the adjacent layers. To capture the detail of damage behaviors during ballast impact and CABI, a refined mesh area of 125 mm × 75 mm at the vicinity of the impact location (the specimen's center) was modeled with the element size of 1.25 mm, while the remaining areas were meshed with the element size of 2.5 mm (Fig. 6).

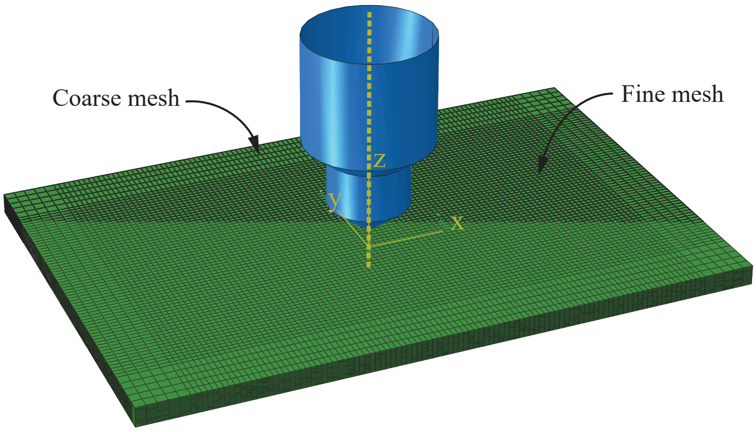

Figure 6: FE model used for a single ballast impact simulation.

The conical impactor was assumed as a rigid body in the simulation. Appropriate mass and initial velocity were prescribed to the impactor, while the composite laminates were fully clamped according to the standard testing method. During the ballast impact, contact was simulated using penalty algorithm within Abaqus/Explicit [41]. Wherein, the contact was established by normal pressure allowing the frictional force to arise throughout the ballast impact. Friction was introduced between all the contact pairs using the built-in penalty function in Abaqus/Explicit [41]. The friction coefficient was set as 0.3 for all contacts to have a reliable accuracy and computational performance.

Subsequently, the impacted model of the laminates containing all the damage history and internal stresses, has been transfered to the CABI simulation. The boundary conditions for the CABI were set as shown in Fig. 5b, where the rigid fixture assembly was used to impose the compression displacement. The bottom fixture was fixed with an encastre boundary condition, and a compression displacement of 1.5 mm was applied to the top fixture.

4. Results and discussion

4.1. Ballast impact tests on CFRP laminates

Numerical simulations of single and repeated ballast impacts have been performed to investigate the damage behaviors of CFRP laminates caused by the ballast impacts. The single ballast impacts are implemented with various impact energies, while repeated ballast impacts on the same site or different sites are considered for the later case. Impact responses, are characterized based on the history curves of impact force and damage dissipation energy, as well as delamination area of each ply of CFRP laminates to evaluate the effect of impact energy and number of impacts on the damage behaviors.

4.1.1. Single ballast impact

Five instantaneous impact velocities of 18.26 m/s, 25.82 m/s, 31.63 m/s, 36.51 m/s and 40.82 m/s are assigned to the conical impactor to obtain the impact energies of 10 J, 20 J, 30 J, 40 J and 50 J, respectively. History curves of impact force and damage dissipation energy of CFRP laminates during single ballast impacts with various impact energies are depicted in Figs. 7a and b, respectively.

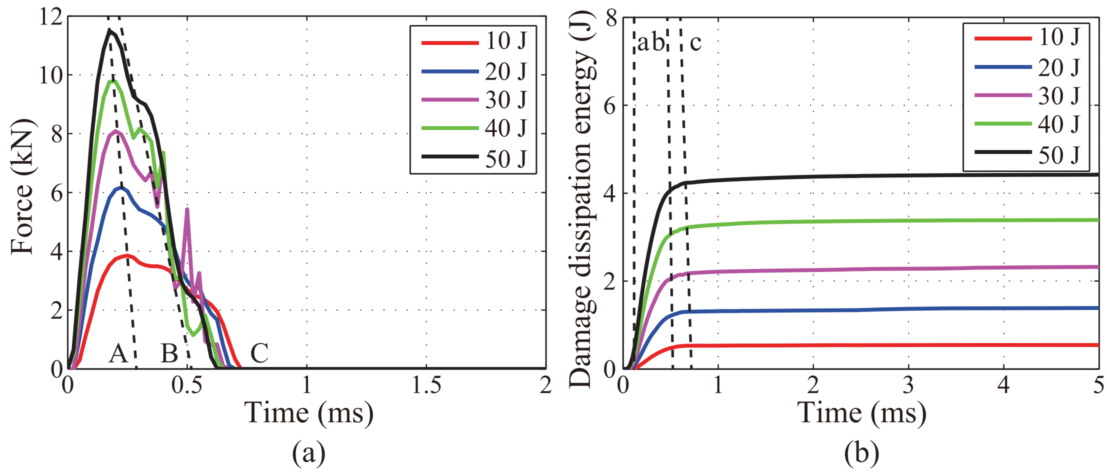

Figure 7: Predicted history curves of: (a) impact force and (b) damage dissipation energy of CFRP laminates obtained during single ballast impacts with various impact energies.

The dynamic impact response and damage initiation are well captured during numerical simulations. As shown in Figs. 7a and b, the impact force and damage dissipation energy rise steadily with the increase of impact energy. Moreover, the impact force peaks (corresponding to point A in Fig. 7a) and the two drops of force (immediately after points A and B in Fig. 7a) are observed. Together with the damage dissipation energy of CFRP laminates (Fig. 7b), the first force drop (after point A in Fig. 7a) is identified as the initiation of delamination (after point a in Fig. 7b) , while the second one (after point B in Fig. 7a) corresponds to fiber breakage, matrix cracking and the growth of delamination (i.e. after point b in Fig. 7b).

The onset of impacts happens almost at the same time, then the impact forces begin to increase. After they reach the maximum forces, they rapidly decrease back to zero at different times of 0.725 ms, 0.710 ms, 0.660 ms, 0.645 ms and 0.625 ms for the impact energies of 10 J, 20 J, 30 J, 40 J and 50 J, respectively. It explains that the initial impact energy in each case is significantly diverse, and the final damage dissipation energy reaches the converged value at different time for each case. Therefore, the dashed line going through point c (Fig. 7b), which corresponds to the end of impact, is not perpendicular to the x-axis.

Predicted total interlaminar and intralaminar damage dissipation energies of CFRP laminates are shown by the line graphs in Figs. 8 and 9. Clearly, both total energy dissipations due to inter-

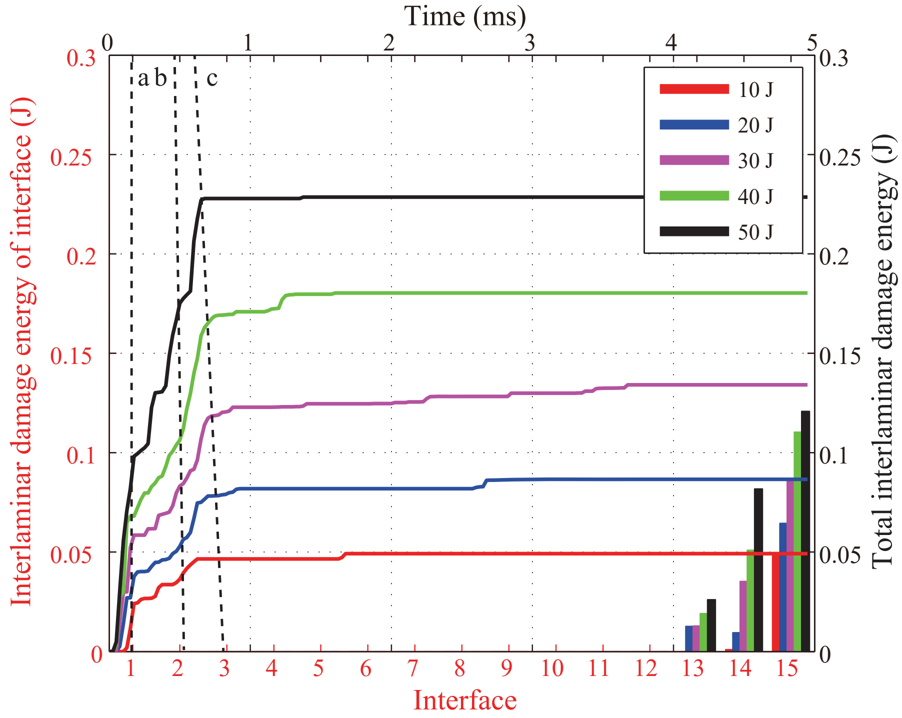

Figure 8: Predicted interlaminar damage dissipation energy of each interface (bar graph referring to the primary x-y axis in red) and the total interlaminar damage energy released by the CFRP laminates (line graph referring to the secondary x-y axis in black) against time, obtained during single ballast impact tests with various impact energies. Interface-15 corresponds to the one nearest to the impacted side.

laminar and intralaminar damages are increased with the growth of impact energy. By comparing the total interlaminar damage energy in each case (Fig. 8), it indicates that the delamination first occurs at the onset of impact (corresponding to point a in Fig. 8). During the progression of the impact, various sudden increasing steps appear in the curves (after point a in Fig. 8) and they correspond to the delamination of different interfaces at various times. Finally, the total interlaminar damage energies (after point c in Fig. 8) reach to 0.049 J, 0.087 J, 0.134 J, 0.180 J and 0.229 J for the impact energies of 10 J, 20 J, 30 J, 40 J and 50 J, respectively.

Advent of delamination between the adjacent layers, intralaminar damage initiates in the impacted layer, and accumulates rapidly in the though-thickness direction (after point a in Fig. 9). Moreover, as the impactor penetrates deeply inside the laminates (after point b in Fig. 9), the intralaminar damage resulting from fiber breakage and matrix cracking becomes the dominant failure mechanism. CFRP laminates ultimately absorb the total intralaminar energies of 0.497 J, 1.300 J, 2.187 J, 3.208 and 4.192 J (after point c in Fig. 9) during each ballast impact test from 10 J to 50 J, respectively.

Similarly, Figs. 8 and 9 (bar graphs) also show the intralaminar and interlaminar damage energies dissipated by each interface and layer, respectively. Among these layers and interfaces, the layer-16 is on the impacted side, and interface-15 is between the layer-15 and 16. Throughout the ballast impact process, delamination initially occurs at interface-15. Then, the adjacent two interfaces are damaged in most cases (except 10 J) before the impact process ends. This prediction

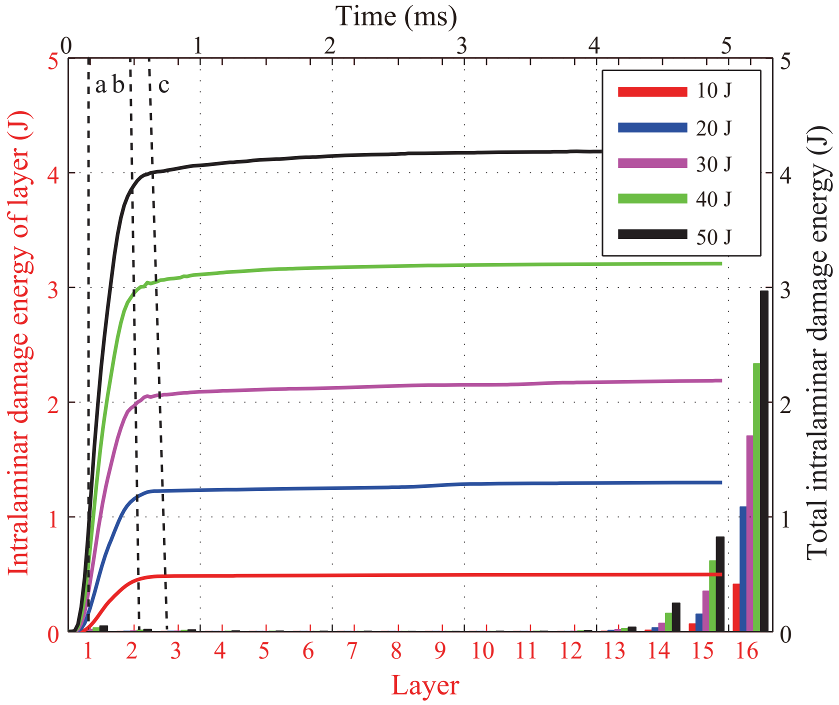

Figure 9: Predicted of intralaminar damage dissipation energy of each layer (bar graph referring to the primary x-y axis in red) and the total intralaminar damage energy released by the CFRP laminates (line graph referring to the secondary x-y axis in black) against time, obtained during single ballast impact tests with various impact energies. Layer-16 is located on the impacted side.

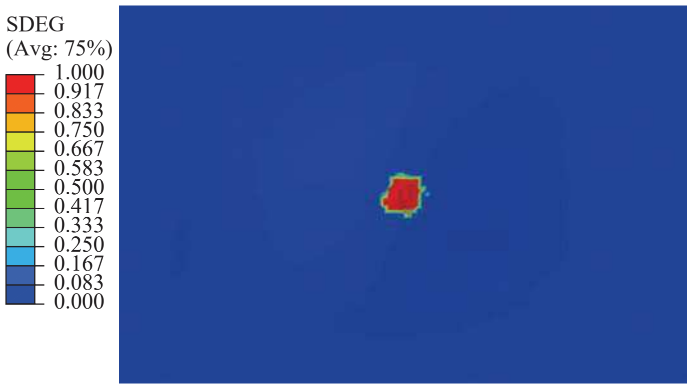

Figure 10: Projected delamination area (SDEG) of interface-15 obtained from the numerical simulation with the impact energy of 50 J.

agrees well with the different increasing steps in the total interlaminar damage dissipation energy curves (line graph in Fig. 8), and those steps are due to the progressive delamination of different interfaces. Moreover, from the comparison between interlaminar damage dissipation energy of each interface, it is found that more than 85.4% of the total interlaminar damage energy is dissipated by the interface-15 and 14, while those beneath interface-13 are not significantly affected by these impact energies. In contrast, intralaminar damage occurs in most of the top and bottom layers of CFRP laminates, as shown in Fig. 9. Besides, the upper layers (layers 16-14) dissipated approximately 96.4% of the total intralaminar damage energy.

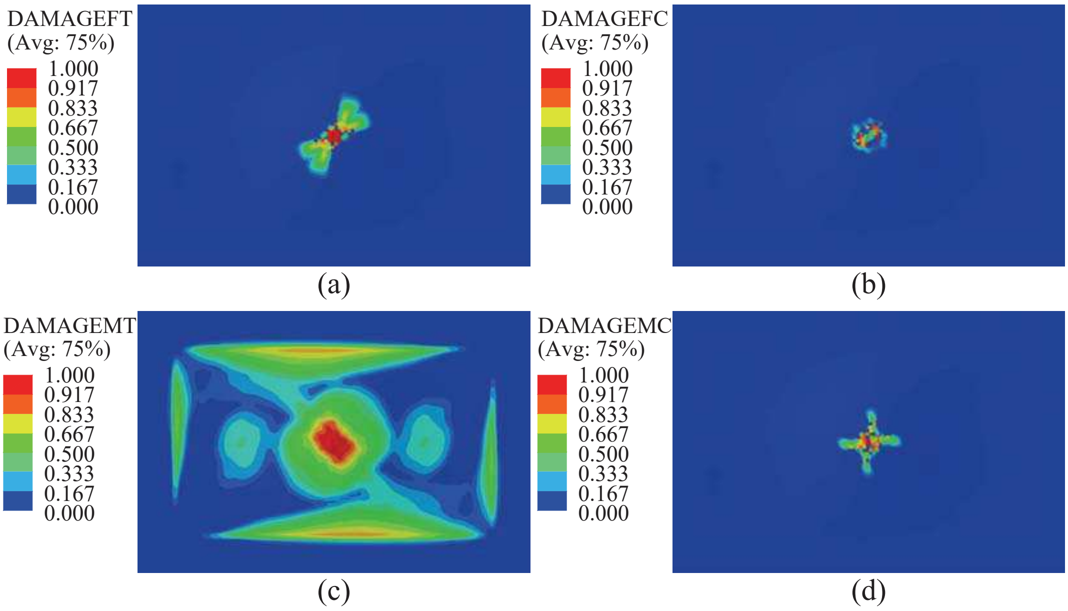

Figure 11: Projected intralaminar damage areas of layer-16 obtained from the numerical simulation with the impact energy of 50 J corresponding to the damages of: (a)fiber-tensile, (b) fiber-compressive, (c) matrix-tensile and (d) matrix-compressive.

To further understand the damage behaviors within the CFRP laminates, the projected areas of interlaminar and intralaminar damages from the numerical simulation with the impact energy of 50 J are plotted for interface-15 and layer-16 in Figs. 10 and 11, respectively. Despite element deletion was not considered during the numerical simulation, the damages are still visible, and they are represented using the projected damage areas. An enclosed delamination area of 86.34 mm^2 (red color contour in Fig. 10) is caused by the ballast impact at the center of interface-15. Moreover, the projected damage areas of layer-16 corresponding to fiber-tensile, fiber-compressive, matrix-tensile and matrix-compressive damages are shown in Fig. 11a-d, respectively. These contours clearly indicate that all four damage mechanisms occur within the CFRP laminates, while the matrix tensile damage is the dominant mechanism. All these damages mainly appear around the impact point while the matrix tensile damage also extend to the vicinity of the specimen's fixture. Hence, these observation reveals that the main damage mechanisms arising from the ballast impact are delamination and matrix tensile damage.

4.1.2. Repeated ballast impacts

In fact, ballast impacts repeatedly occur on the train carbody during the service life. However, most of the recent studies in literature only addressed the single impact and provided minimum consideration to the effect of multi-site impacts. Hence, repeated ballast impacts, in which each impact is assigned with the impact energy of 25 J (impact velocity: 28.87 m/s), are performed at the same site and different sites of the specimen, as shown in Fig. 12. Although the multi-site impact case only considers the impact energy of 25J per impact, repeated impacts leading to the total impact energy of 50J, have been compared with the single impact case of 50J.

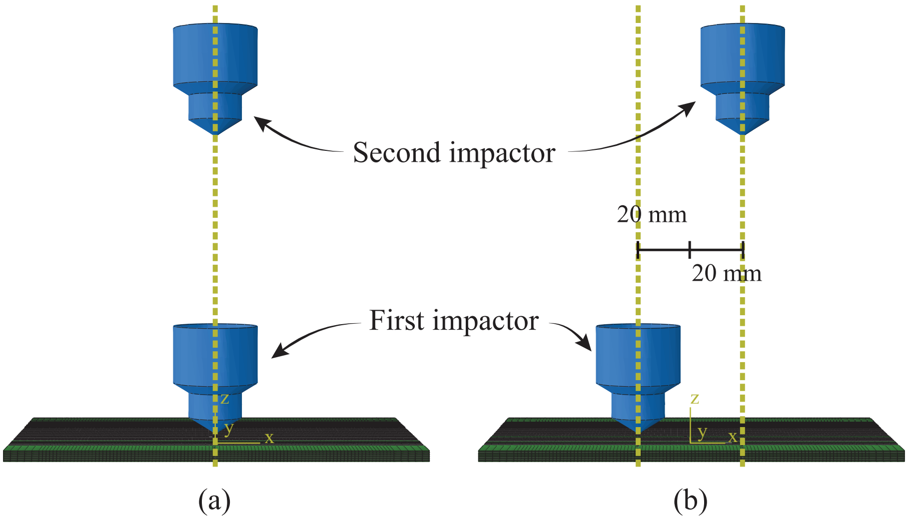

Figure 12: Numerical models used for the repeated ballast impact simulations at the (a) same site and (b) different sites of CFRP laminates.

In the case of repeated ballast impacts on the same site (Fig. 12a), while the first impactor contacting at the center of the specimen, the second one is released from the height of 144.34 mm to impact on the same site. After 0.05 ms, when the first ballast impact completely terminates, the corresponding impactor is removed from the numerical simulation, and the second one begins to cause further damage on the specimen. In the second case, the first impactor hits the specimen at a location 20 mm away from the center (along the negative x axis). The second impactor is released from the same height to impact symmetrically (20 mm from the center along the positive x axis) to the first impactor, as illustrated in Fig. 12b.

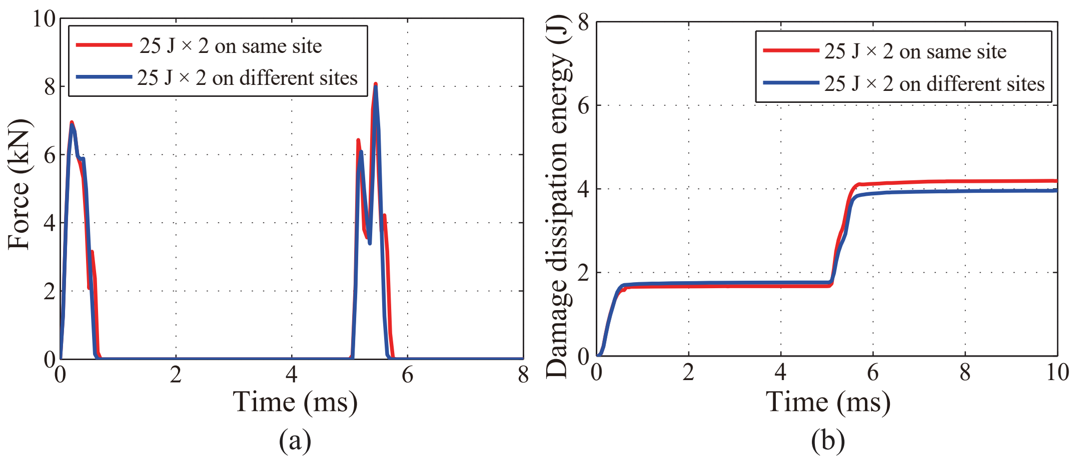

Figure 13: Predicted history curves of: (a) impact force and (b) damage dissipation energy of CFRP laminates obtained from the repeated ballast impacts on the same site and different sites.

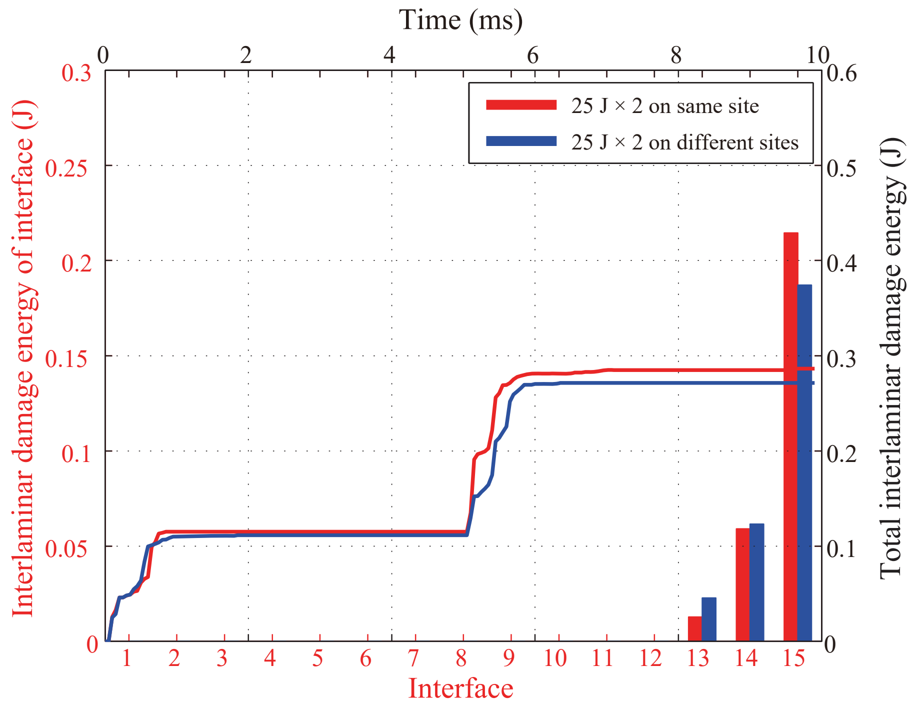

Figure 14: Predicted interlaminar damage dissipation energy of each interface (bar graph referring to the primary x-y axis in red) and the total interlaminar damage energy dissipated from the CFRP laminates (line graph referring to the secondary x-y axis in black) against time for the repeated ballast impacts on the same site and different sites. Interface-15 corresponds to the one nearest to the impacted side.

Figs. 13a and b show the history curves of impact force and damage dissipation energy of CFRP laminates for the repeated ballast impacts on the same site and different sites, respectively. Two principal fluctuations of impact force appearing due to the repeated impacts are thoroughly captured in the history curves as shown in Fig. 13a. In both cases, the force peak associated to the second impact (approximately 8.04 kN) is 16.4% higher than that of the first one (approximately 6.91 kN). Likewise, two increasing steps appear in the damage dissipation energy curve for each repeated impact case as shown in Fig. 13b. At the end of the first increasing step, the damage energies of 1.67 J and 1.76 J are dissipated by the first impact in the cases of the same site and different sites, respectively. There exists a difference of 5.4% between these two cases, in which the specimen of the first case absorbs more energy than that of second one. This difference is mainly caused by the different impact locations on the specimen.

At the end of second increasing step, the composite laminates dissipate 4.19 J and 3.95 J for the case of repeated impacts on the same site and different sites, respectively. Comparing with the results of first impact in both cases, the second impact dissipates relatively more damage energy. Moreover, the different site case releases lower total energy compared to the same site one, and this is primarily attributed to the effect of progressive damages caused by the second impact after the first impact on these specimens. Although interlaminar and intralaminar damages are introduced in both cases, 40 mm distance exists between the repeated impacts at different sites while the damage area overlaps during the repeated impacts on the same site. Thus, the same site impact

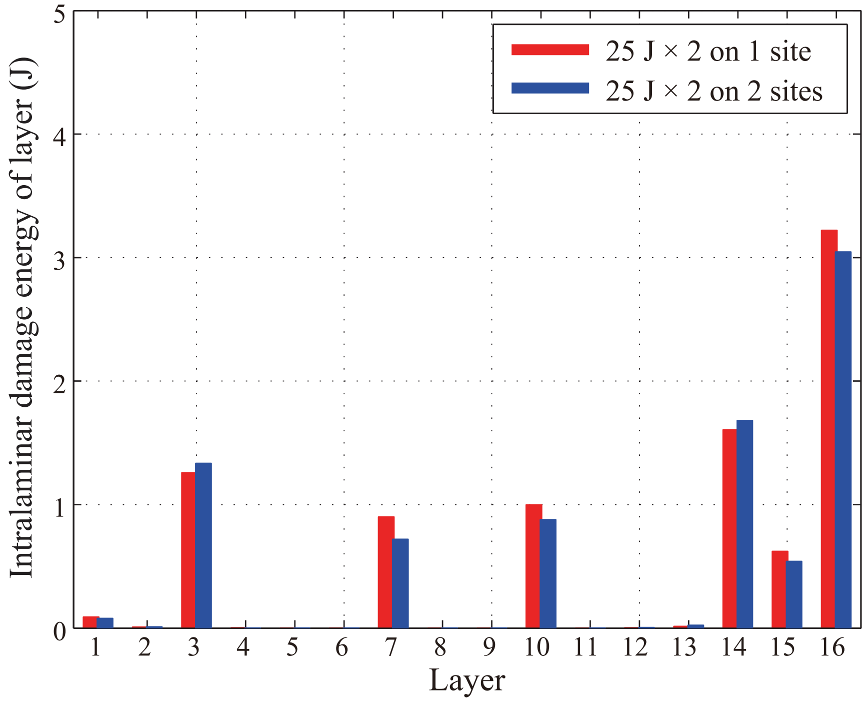

Figure 15: Predicted intralaminar damage dissipation energy of each layer (bar graph referring to the primary x-y axis in red) and the total interlaminar damage energy dissipated from the CFRP laminates (line graph referring to the secondary x-y axis in black) against time for the repeated ballast impacts on the same site and different sites. Layer-16 is located on the impacted side.

case significantly increases the damage energy dissipation during the second ballast impact.

Line graphs in Figs. 14 and 15 show the predicted total interlaminar and intralaminar damage dissipation energies of CFRP laminates. During the first ballast impact of the same-site and different-site cases, CFRP laminates respectively dissipates the total delamination energy of 0.115 J and 0.111 J due to the interlaminar damage. Subsequently, the second impact causes more serious delamination to the laminates of the same site case (0.285 J) than that of the different sites case (0.271 J), as shown in Fig. 14. The history curve of total intralaminar damage dissipation energy corresponding to the same site case initially increases to 1.554 J after the first impact, which is slightly lower than that of the different sites case (1.648 J). However, after the second impact, the history curve of the same site case reaches 3.900 J which is higher than that of the different sites case (3.681 J). This inversion is clearly caused by the overlap of the damage areas resulting from the two ballast impacts on the same site.

In addition, the bar graphs in Figs. 14 and 15 illustrate the predicted dissipation energy of each interface and layer due to interlaminar and intralaminar damages, respectively. For both interlaminar and intralaminar damages, the dissipation energy during repeated impacts is comparable with single impact tests, i.e. only the upper three interfaces and layers are clearly damaged. Despite the delamination of interface-15 of the same site case dissipates more energy than that of the different sites case, interlaminar damage energy dissipation is in contrary for the interface-14 and interface-13. Moreover, the similar dissipation energy distribution of each layer appears for the intralaminar

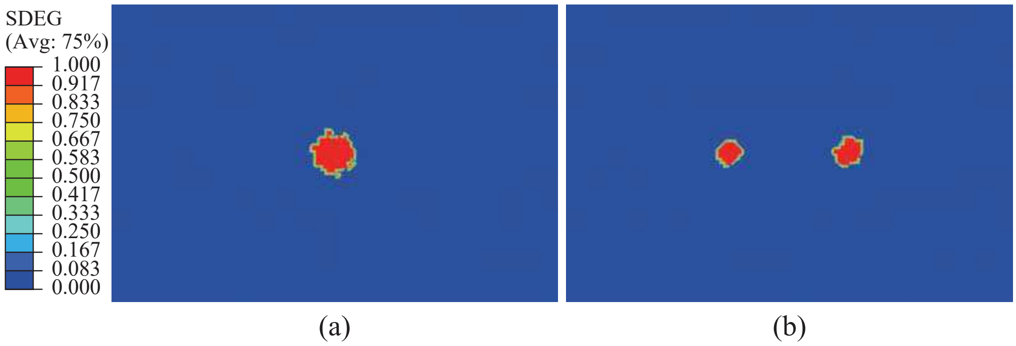

Figure 16: Projected delamination area of interface-15 from the numerical simulation with repeated ballast impacts of 25 J × 2 on the same site.

damage. It explains that, layer-16 and layer-15 around the second impact point significantly deteriorate the load bearing capability during the first impact, while the influence on the lower layers are relatively smaller. Due to this obvious reduction of the impact-resistance of layer-16 and layer-15, the second ballast impact in the same site case expands the damage area associated with the first impact in a nonlinear manner. Meanwhile, as the interlaminar and intralaminar damages propagate in the thickness direction, the impact-resistance of lower interfaces and layers are rarely affected by the first impact. However, since the second impact occurs at an undamaged area of the laminates in the different sites case, it causes a similar damage area compared to the first one, so that the damage areas increase in an approximately linear manner. Nevertheless, this behavior could be affected by the distance between the first and second impact points during the different-site impacts.

Fig. 16 shows the projected delamination areas of interface-15 obtained from the numerical simulations of both repeated-impact cases. The repeated impacts result to the damage area of 159.679 mm^2 and 129.706 mm^2 at interface-15 for the same-site and different-site cases, respectively. Although two delamination areas are found within interface-15 for the different-site case, the total damage area is 18.8% less than that of the same-site case. This difference also supports the earlier discussion for the dissimilarity of the damage energy dissipated by interface-15 (Fig. 14). Furthermore, no delamination is observed between those two delamination areas in Fig. 16b, which means the second impact has experienced negligible effect of the first one during the repeated impacts at different sites.

The projected intralaminar damage areas of layer-16 obtained from the numerical simulations of the two repeated-impact cases are shown in Fig. 17. All four interlaminar damage modes appear within layer-16 during the repeated-impact tests. The matrix-tensile damage dominates the intralaminar damage in both cases, which predicts the possibility of the matrix cracking within the composite layer as the principal damage mechanism. Besides, by comparing the damage areas caused by repeated impacts in the different-site case, the second ballast impact (the damage areas on the +x side) causes relatively larger damage, especially noticeable for the matrix-tensile and matrix-compressive damages. This effect can also be attributed to the reduction of impact-resistance of layer-16 due to the first ballast impact as presented in Fig. 15.

To further understand the effect of repeated ballast impacts, these two cases are also compared

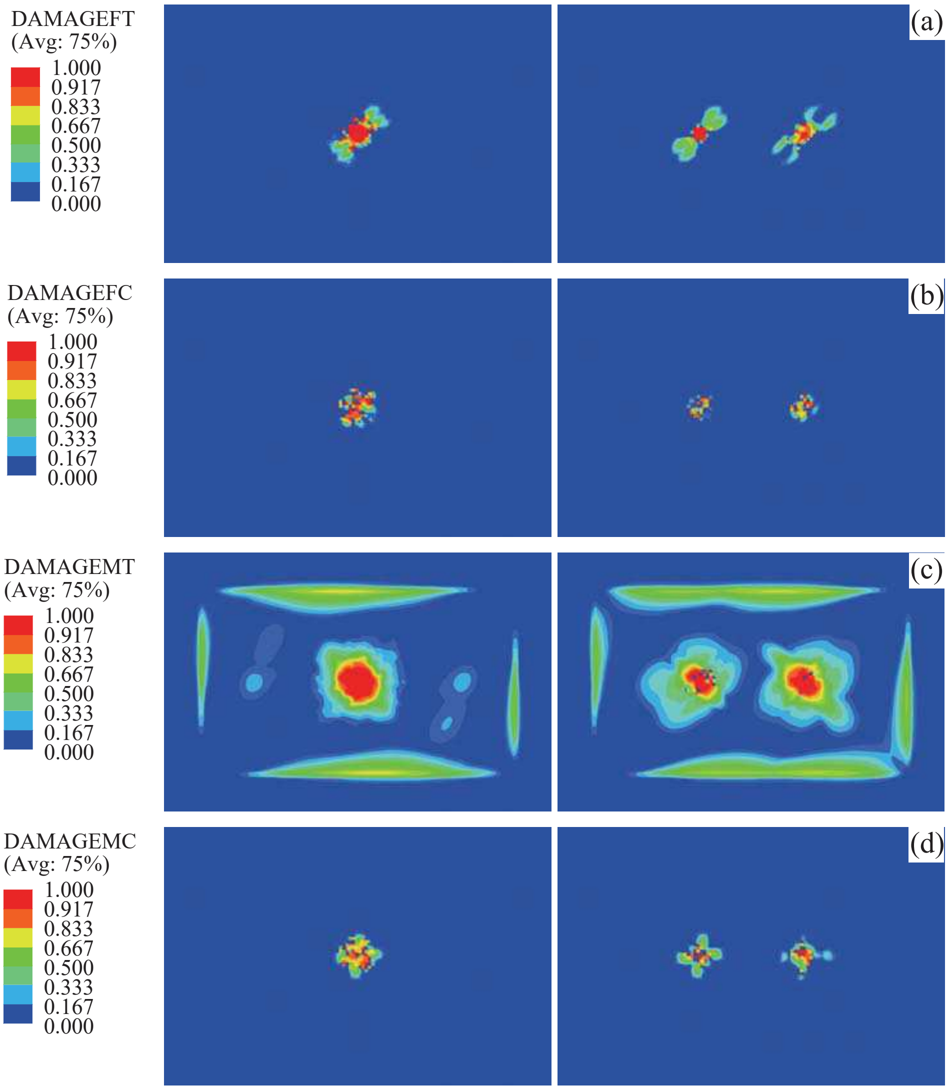

Figure 17: Projected areas of layer-16 from the numerical simulation with repeated ballast impacts of 25 J $\times$ 2 on the same site (left) and different sites (right) for the intralaminar damages of: (a) fiber-tensile, (b) fiber-compressive, (c) matrix-tensile and (d) matrix-compressive.

with the single impact with the energy of 50 J, while the total impact energies are kept equal in all cases. During the single impact case (with 50 J), the specimen dissipates almost the same total damage energy, which is equal to the total damage dissipation energy of the repeated impacts. Moreover, the comparison indicates that, more interlaminar damage energy is dissipated by the whole CFRP laminates and especially by the upper layers during the repeated-impact tests. In contrast, relatively less intralaminar damage is caused by the repeated impacts. The comparison of the projected interlaminar and intralaminar damage areas also exhibites the same trend.

4.2. Compression after ballast impact (CABI) on CFRP laminates

After the single and repeated ballast impacts, simulation of CABI tests have been performed on the impacted specimens using the loading conditions described in Section 3.3. This section focuses on the mechanical responses of the damaged CFRP laminates, including force-displacement curves, residual compressive strength after CABI and damage behaviors.

4.2.1. Compression after single ballast impact

Initially, CABI simulations are carried out on the single blast impacted specimens with various impact energies. To study the reduction of compression strength due to the ballast impact, a reference compression test is also implemented using an intact specimen. The force-displacement cuvres of CABI and compression of pristine laminates are depicted as shown in Fig. 18.

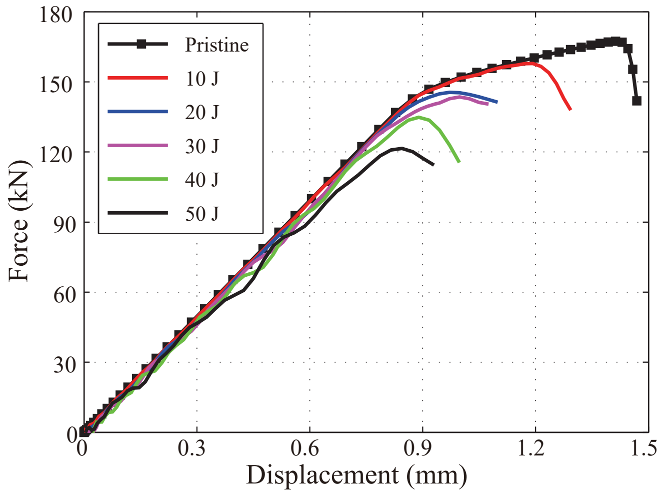

Figure 18: Predicted force-displacement curves extracted from the numercial simulations of CABI and compression on impacted and pristine laminates.

During the numerical CABI and compression simulations, the force is obtained from the fixtures at the boundaries of the laminates. Due to the existence of damages on the impacted laminates, especially those impacted with high initial energies, obvious oscillations are observed within the compression force response with the progressive displacement. Both impacted and intact specimens are completely failed before the simulation reaches the maximum prescribed displacement. The predicted maximum compression loads are used to compute the pristine and residual compressive strengths, as listed in Table 3. Moreover, a strength reduction factor given by the ratio between the residual and pristine compressive strength values, is proposed to evaluate the loss of compressive strength due to the ballast impacts with different initial energies.

Table 3: Numerical results from the simulations of compression and CABI on pristine and damaged laminates after single ballast impacts.

Impact energy (J)	0	10	20	30	40	50
Compressive strength (MPa)	348.67	328.86	304.10	298.77	287.10	276.16
Strength reduction factor	-	5.68%	12.78%	14.31%	17.66%	20.80%

These results show that, the residual compressive strength decreases in a nonlinear manner with the increase of ballast impact energy. Especially, compressive strength after impact reduces fiercely at low impact energies of 10 J and 20 J. It highlights that the remaining compressive strength is more sensitive to the appearance of damages due to ballast impact than the severity of the damage for the impact energy range from 10 to 50 J. Thus, it is important to take safety measures at early stage of impact on CFRP laminates irrespective of the severity of the impact.

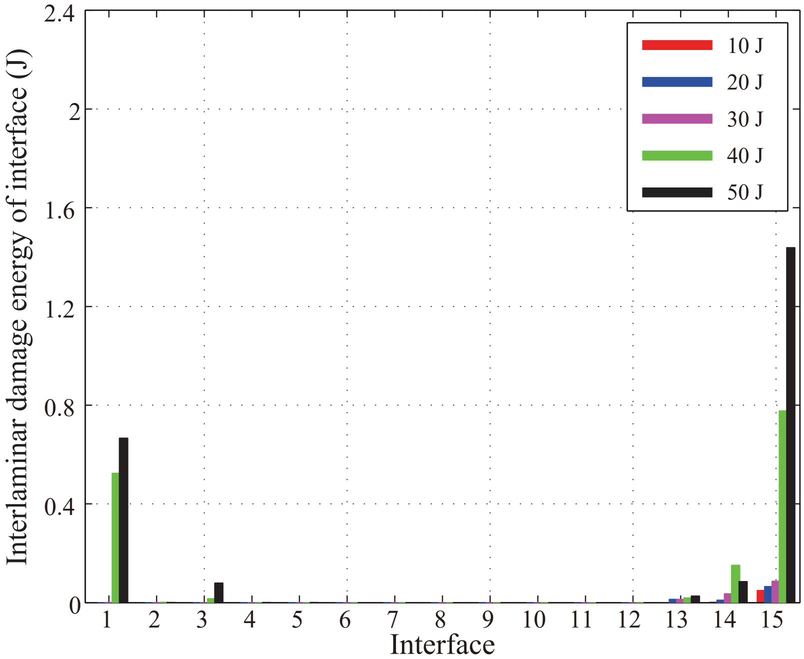

Figure 19: Predicted interlaminar damage dissipation energy of each interface from CABI tests with various impact energies, at the compressive displacement of 0.944 mm. Interface-15 is the nearest one to the impacted side.

Figs. 19 and 20 show the predicted interlaminar and intralaminar dissipation energies of each interface and layer respectively at the compressive displacement of 0.994 mm, where approximately same work done on all specimens due to the compression (Fig. 18). The comparison of results in Figs. 8 and 19 clearly shows that, delamination is prone to significantly increase within the interfaces near the top and bottom edges of the impacted specimen with the progression of compressive load. While, slight delaminations appear within the intermediate interfaces during the compression. Moreover, the damage resulting from the ballast impacts with energies of 40 J and 50 J, leads the subsequent compression to cause more delamination, especially within the interface-1 (the lower one) and interface-15 (the upper one on the impacted site).

From the results of energy dissipated by the intralaminar damage in Figs. 9 and 20, significant increase of dissipation energy occurs in the staggered layers, which mainly consist of layer-1, 3, 7, 10, 14 and 16. The carbon fibers in these layers, except for layer-1 and layer-16 are oriented in 0° direction (parallel to the compression direction). Therefore, we can conclude that, the fibers in 0° direction accommodates the majority of load during CABI simulation.

The projected interlaminar damage area of interface-15 is obtained from the CABI simulation at the compressive displacement of 0.944 mm, to study the effect of single ballast impact on the damage modes and growth (Fig. 21). It is clearly found that, the delamination due to the compression does not propagate in the vicinity of the previous delamination associated with the

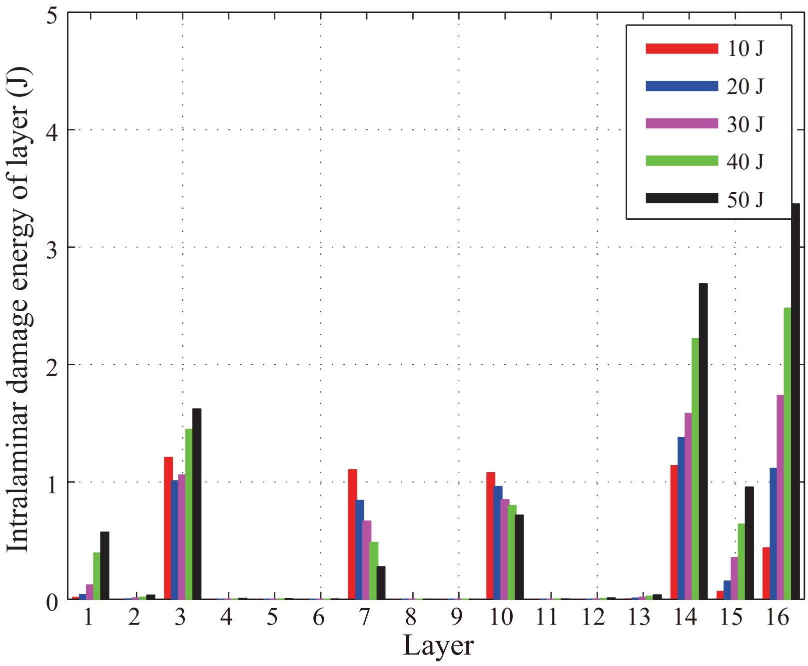

Figure 20: Predicted intralaminar damage dissipation energy of each layer from CABI tests with various impact energies, at the compressive displacement of 0.944 mm. Layer-16 is located on the impacted side.

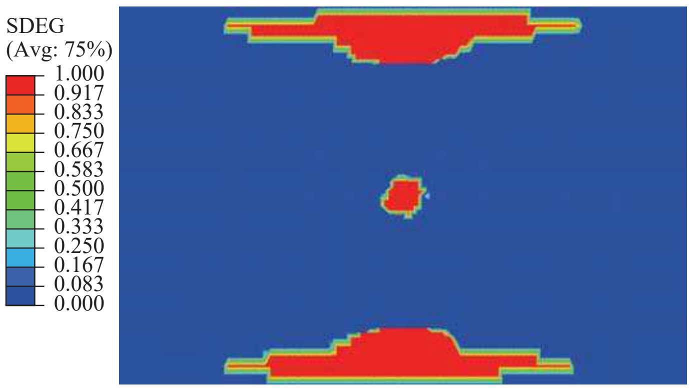

Figure 21: Projected delamination area of interface-15 extracted from the numerical CABI simulation with the impact energy of 50 J at the compression displacement of 0.944 mm.

ballast impact. Nonetheless, the subsequent delamination first appears nearby the top and bottom edges of the laminates. And then they continuously grow towards the specimen center until the complete failure.

According to the aforementioned finding, the fibers in 0° direction mainly accommodate the compression load, while few impact damages are found particularly within the neighboring layers on the impacted side. Hence, projected areas of different damage modes are shown in Fig. 22 for layer-16 to analyze the effect of ballast impact. Similar behaviors are observed for fiber-compressive and matrix-tensile damages, as shown in Figs. 22b and c. Especially, the matrix-tensile damage rapidly extends with the previous damage caused by the ballast impact. It indicates

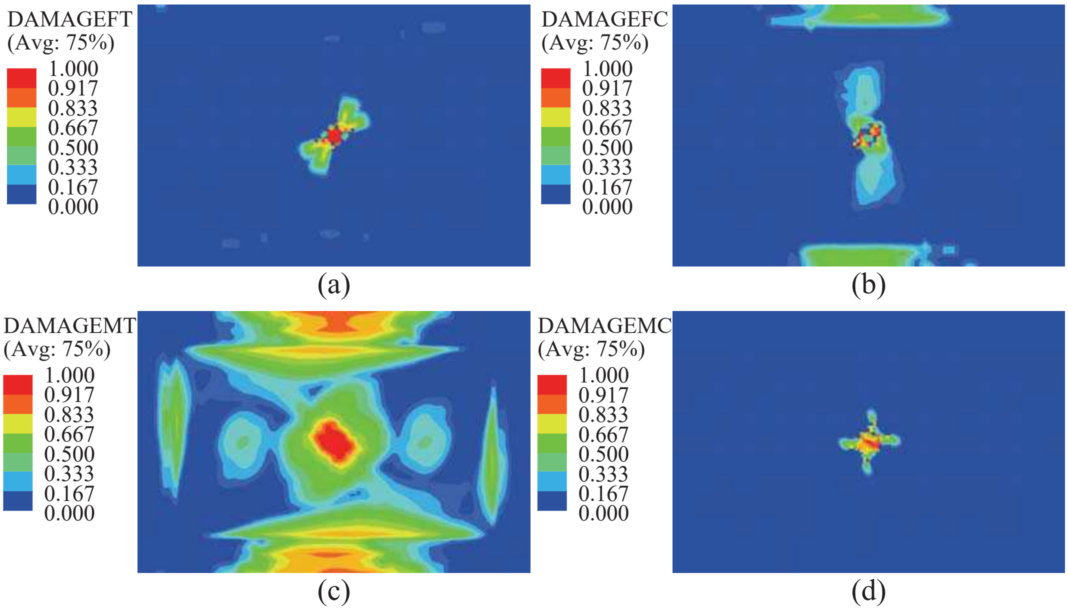

Figure 22: Projected (a) fiber-tensile, (b) fiber-compressive, (c) matrix-tensile and (d) matrix-compressive damage areas of layer-16 extracted from the numerical CABI simulation with the impact energy of 50 J at the compression displacement of 0.944 mm.

that, the matrix of layer-16 is likely to fully fail in matrix-tensile damage mode under the progressive compressive load. The matrix-tensile damage resulting from the folding of the specimen surface, is considered as the dominant damage mechanism. In addition, the growth and propagation of fiber-tensile (Fig. 22a) and matrix-compressive (Fig. 22d) damages are relatively low during the CABI. However, significant fiber-compressive damage is predicted in the layers where fibers are oriented in 0° direction. This observation also supports that the layers containing 0° direction fibers mainly accommodate the load during the compression.

4.2.2. Compression after repeated ballast impacts tests

CABI simulations are also performed for the CFRP laminates which were damaged by repeated ballast impacts. Fig. 23 shows the predicted force-displacement curves obtained from the numerical CABI simulations. Sudden force drop has been also observed after the appearance of force peak in each case, and it indicates the failure.

Table 4: Numerical results extracted from the simulations of compression and CABI on pristine and damaged laminates after repeated ballast impacts.

Impact energy (J)	0	25 × 2 (on same site)	25 × 2 (on different sites)
Compressive strength (MPa)	348.67	292.71	299.24
Strength reduction factor	-	16.05%	14.18%

Similar to the single impact cases, the reduction of compressive strength is estimated based on the loss of CABI strength of repeatedly impacted laminates (using force-displacement response) compared to the pristine laminates. The calculated compressive strengths and reduction factors

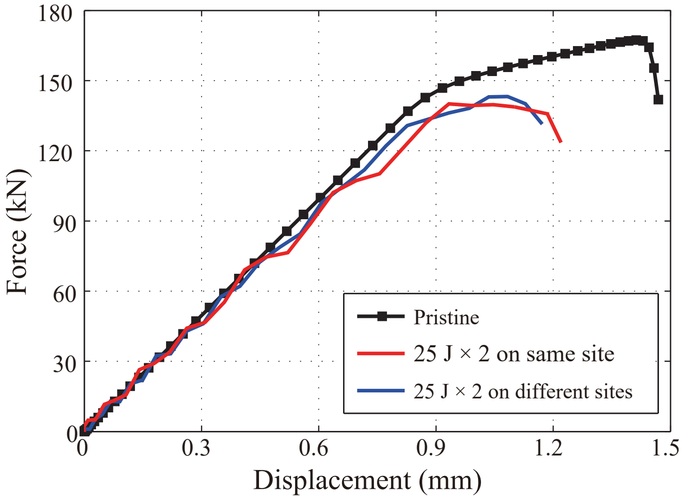

Figure 23: Predicted force-displacement curves extracted from numercial simulations of CABI and compression on multi-impacted and pristine laminates.

are listed in Table 4. Moreover, it clearly reveals that, the damages caused by the repeated impacts on the same-site reduce the compressive strength of the CFRP laminates more significantly than that of the different-site case. While, the compressive strength of each repeated-impact case is relatively higher than that of the single ballast impact with the energy of 50 J. Furthermore, the same damage initiation and growth mechanisms are observed during the CABI simulation of laminates damaged by repeated ballast impacts as similar to the single impact cases. Therefore, if one impact is divided into two or more impacts, less harmful effect is caused for the same total impact energy. In addition, the number of impact site affects the damage distribution and the compressive strength after ballast impact.

Additionally, the specimens subjected to repeated impacts of 2×25J (having total absorbed energy for same-site case: 4.19J and the different-site case: 3.95J) absorbed less impact energy than that subjected to single impact of 50J (4.42J). Wherein, the intralaminar damage dissipation energies are 3.90J and 3.68J for the repeated impacts on the same site and different sites, respectively. These values are relatively less than that of the single impact of 50J (4.192J). This obvious difference of intralaminar damage dissipation energy caused a significant reduction of the compressive strength for the single-impacted laminates (20.80%) than the repeated-impacted ones (same-site case: 16.05%; different-site case: 14.18%). Therefore, it reveals that the compressive strength is more sensitive to intralaminar damages compared to interlaminar damages.

5. Conclusions and perspectives

In this study, numerical simulations of ballast impact and CABI were investigated for the CFRP laminates used in the design and manufacturing of train carbodies, to identify the damage mechanisms and residual compressive strength after impact. To ensure the computational efficiency and accuracy, 3D shell elements along with zero-thickness cohesive elements were used to establish the models of CFRP laminates.

Numerical simulations performed with various impact energies reveal that the delamination initially emerges near the impacted side. Then, fiber breakage, matrix cracking and progressive delamination occur in thickness direction until the laminates completely fail. Moreover, both the interlaminar and intralaminar damage dissipation energies rise with the increase of impact energy. The projected interlaminar and intralaminar damage areas disclose that the final stage of ballast impact is dominated by the delamination and matrix-tensile damage.

Subsequently, compression simulations were performed on these impacted laminates to identify the residual compressive strength. The residual compressive strength decreased in a nonlinear manner with the increasing impact energy. It was found that the CABI simulation is more sensitive to the presence of impact damages rather than the damage intensity. The results obtained for the damage dissipation energies reveal that, the layers whose fiber orientation is in 0° direction accommodate large proportion of load during compression. Moreover, new delamination and matrix-tensile damages appear along the top and bottom edges of the CFRP laminates.

Repeated ballast impacts on the same site and different sites of CFRP laminates are investigated to study the effect of multiple-impacts. For a given total impact energy, the repeated impacts result with more delamination while having less intralaminar damages compared to the single impact. The repeated impacts on different sites show relatively less detrimental damage to the CFRP laminates compared to the repeated impacts on the same site. Moreover, the results obtained from the CABI simulations on these repeatedly impacted laminates indicate that the number of impact site significantly affects the residual compressive strength. A lower reduction factor of compressive strength is obtained for the repeated impacts at different sites.

Although only the vertical ballast impacts ($\theta = \pi/2$) have been investigated in this study, the non-vertical ones are more likely to occur in realistic cases. Considering the angle between the directions of train movement and flying ballast is of great importance that will help to understand the shear damage mechanism during high speed ballast impact for CFRP laminates. The extension of the proposed protocol will systematically be investigated for the non-vertical ballast impacts. Furthermore, the set-up of an experimental system for high-velocity ballast impact meets two key challenges that requires: (i) a precise control of the ballast impactor, (ii) a robust measurement of impact responses (i.e. impact force and energy) for CFRP laminates. A reliable testing platform for high-velocity ballast impact test is also required to possess an appropriate air gun machine with additional relatively high-speed acquisition devices. These challenges will be untangled in our future work to completely understand the damage behaviors of composite laminates during high-speed impacts.

Acknowledgements

Authors acknowledge the financial support from National Natural Science Foundation of China (NSFC, U1833116 and 11902251), China Postdoctoral Science Foundation (2018M642775). This study is also supported by European Commission under the project REFRESCO (Grant agreement no. 605632) and Key Scientific Research Project of Colleges and Universities in Henan Province (20A460003). TS acknowledges F.R.S.-FNRS (Belgium) during his postdoc at UCLouvain.

Data Availability Statement

The raw/processed data required to reproduce these findings cannot be shared at this time as the data also forms part of an ongoing study.

References

[1] K. B. Shin, S. H. Hahn, Evaluation of the structural integrity of hybrid railway carriage structures including the ageing effects of composite materials, Composite structures 68 (2) (2005) 129–137.

[2] J.-S. Kim, J.-C. Jeong, Natural frequency evaluation of a composite train carbody with length of 23 m, Composites Science and Technology 66 (13) (2006) 2272–2283.

[3] J.-S. Kim, S.-K. Chung, A study on the low-velocity impact response of laminates for composite railway bodyshells, Composite Structures 77 (4) (2007) 484–492.

[4] J.-S. Kim, S.-J. Lee, K.-B. Shin, Manufacturing and structural safety evaluation of a composite train carbody, Composite Structures 78 (4) (2007) 468–476.

[5] A. Zinno, E. Fusco, A. Prota, G. Manfredi, Multiscale approach for the design of composite sandwich structures for train application, Composite Structures 92 (9) (2010) 2208–2219.

[6] A. Önder, M. Robinson, Harmonised method for impact resistance requirements of E-glass fibre/unsaturated polyester resin composite railway car bodies, Thin-Walled Structures 131 (2018) 151–164.

[7] X. Sun, S. Hallett, Failure mechanisms and damage evolution of laminated composites under compression after impact (CAI): Experimental and numerical study, Composites Part A: Applied Science and Manufacturing 104 (2018) 41–59.

[8] L. Xia, D. Da, J. Yvonnet, Topology optimization for maximizing the fracture resistance of quasi-brittle composites, Computer Methods in Applied Mechanics and Engineering 332 (2018) 234–254.

[9] L. Xia, L. Zhang, Q. Xia, T. Shi, Stress-based topology optimization using bi-directional evolutionary structural optimization method, Computer Methods in Applied Mechanics and Engineering 333 (2018) 356–370.

[10] Z. Wu, L. Xia, S. Wang, T. Shi, Topology optimization of hierarchical lattice structures with substructuring, Computer Methods in Applied Mechanics and Engineering 345 (2019) 602–617.

[11] L. Meng, W. Zhang, D. Quan, G. Shi, L. Tang, Y. Hou, P. Breitkopf, J. Zhu, T. Gao, From topology optimization design to additive manufacturing: Today's success and tomorrow's roadmap, Archives of Computational Methods in Engineering (2019) 1–26.

[12] R. Ren, J. Zhong, G. Le, D. Ma, Research on intralaminar load reversal damage modeling for predicting composite laminates' low velocity impact responses, Composite Structures 220 (2019) 481–493.

[13] J.-S. Goo, J.-S. Kim, K.-B. Shin, Evaluation of structural integrity after ballast-flying impact damage of a GFRP lightweight bogie frame for railway vehicles, Journal of Mechanical Science and Technology 29 (6) (2015) 2349–2356.

[14] A. Önder, C. ONeill, M. Robinson, Flying ballast resistance for composite materials in railway vehicle carbody shells, Transportation Research Procedia 14 (2016) 595–604.

[15] J. Deng, X. Liu, G. Jing, Z. Bian, Probabilistic risk analysis of flying ballast hazard on high-speed rail lines, Transportation Research Part C: Emerging Technologies 93 (2018) 396–409.

[16] M. Richardson, M. Wisheart, Review of low-velocity impact properties of composite materials, Composites Part A: Applied Science and Manufacturing 27 (12) (1996) 1123–1131.

[17] J. Pernas-Sánchez, J. A. Artero-Guerrero, D. Varas, J. López-Puente, Experimental analysis of normal and oblique high velocity impacts on carbon/epoxy tape laminates, Composites Part A: Applied Science and Manufacturing 60 (2014) 24–31.

[18] Y. Xu, H. Lu, T. Gao, W. Zhang, Predicting the low-velocity impact behavior of polycarbonate: Influence of thermal history during injection molding, International Journal of Impact Engineering 86 (2015) 265–273.

[19] Y. Xu, H. Lu, T. Gao, W. Zhang, Processing-induced inhomogeneity of yield stress in polycarbonate product and its influence on the impact behavior, Polymers 8 (3) (2016) 72.

[20] M. M. Ansari, A. Chakrabarti, Impact behavior of FRP composite plate under low to hyper velocity impact, Composites Part B: Engineering 95 (2016) 462–474.

[21] Y. Tie, Y. Hou, C. Li, X. Zhou, T. Sapanathan, M. Rachik, An insight into the low-velocity impact behavior of patch-repaired CFRP laminates using numerical and experimental approaches, Composite Structures 190 (2018) 179–188.

[22] Y. Hou, Y. Tie, C. Li, T. Sapanathan, M. Rachik, Low-velocity impact behaviors of repaired CFRP laminates: Effect of impact location and external patch configurations, Composites Part B: Engineering 163 (2019) 669–680.

[23] X. Li, D. Ma, H. Liu, W. Tan, X. Gong, C. Zhang, Y. Li, Assessment of failure criteria and damage evolution methods for composite laminates under low-velocity impact, Composite Structures 207 (2019) 727–739.

[24] A. R. Kristnama, X. Xu, D. Nowell, M. R. Wisnom, S. R. Hallett, Experimental investigation of high velocity oblique impact and residual tensile strength of carbon/epoxy laminates, Composites Science and Technology 182 (2019) 107772.

[25] G. Short, F. Guild, M. Pavier, The effect of delamination geometry on the compressive failure of composite laminates, Composites Science and Technology 61 (14) (2001) 2075–2086.

[26] D. Ghelli, G. Minak, Low velocity impact and compression after impact tests on thin carbon/epoxy laminates, Composites Part B: Engineering 42 (7) (2011) 2067–2079.

[27] J. Wang, R. Callinan, Residual strengths of composite structures subjected to ballistic impact, Composite Structures 117 (2014) 423–432.

[28] M. Abir, T. Tay, M. Ridha, H. Lee, Modelling damage growth in composites subjected to impact and compression after impact, Composite Structures 168 (2017) 13–25.

[29] E. González, P. Maimí, E. Martín-Santos, A. Soto, P. Cruz, F. M. de la Escalera, J. S. de Aja, Simulating drop-weight impact and compression after impact tests on composite laminates using conventional shell finite elements, International Journal of Solids and Structures 144 (2018) 230–247.

[30] A. Soto, E. González, P. Maimí, F. M. de la Escalera, J. S. de Aja, E. Alvarez, Low velocity impact and compression after impact simulation of thin ply laminates, Composites Part A: Applied Science and Manufacturing 109 (2018) 413–427.

[31] Z. Zhao, P. Liu, C. Chen, C. Zhang, Y. Li, Modeling the transverse tensile and compressive failure behavior of triaxially braided composites, Composites Science and Technology 172 (2019) 96–107.

[32] H. Tuo, Z. Lu, X. Ma, J. Xing, C. Zhang, Damage and failure mechanism of thin composite laminates under low-velocity impact and compression-after-impact loading conditions, Composites Part B: Engineering 163 (2019) 642–654.

[33] H. Tuo, Z. Lu, X. Ma, C. Zhang, S. Chen, An experimental and numerical investigation on low-velocity impact damage and compression-after-impact behavior of composite laminates, Composites Part B: Engineering 167 (2019) 329–341.

[34] M. Fakoor, S. M. N. Ghoreishi, Experimental and numerical investigation of progressive damage in composite laminates based on continuum damage mechanics, Polymer Testing 70 (2018) 533–543.

[35] W. Tan, B. G. Falzon, L. N. Chiu, M. Price, Predicting low velocity impact damage and Compression-After-Impact (CAI) behaviour of composite laminates, Composites Part A: Applied Science and Manufacturing 71 (2015) 212–226.

[36] NF/F53-695, Installations fixes ferroviaires-Ballasts et gravillons de soufflage-Caractéristiques et spécifications, Association Française de Normalisation, 1996.

[37] D. A. Nistor, Caractérisation du comportement des nouveaux matériaux (composites) sous solicitations d'impact type ballast, Ph.D. thesis, Université Technologie de Compiègne (2011).

[38] J.-C. Quezada, Mécanismes de tassement du ballast et sa variabilité, Ph.D. thesis, Université Montpellier II-Sciences et Techniques du Languedoc (2012).

[39] Z. HASHI, Failure criteria for unidirectional fiber composite, Journal of Applied Mechanics 47 (1980) 3292334.

[40] D. S. Cairns, J. W. Nelson, K. Woo, D. Miller, Progressive damage analysis and testing of composite laminates with fiber waves, Composites Part A: Applied Science and Manufacturing 90 (2016) 51–61.

[41] Hibbitt, Karlsson, Sorensen, ABAQUS/Explicit: user's manual, Vol. 1, Hibbitt, Karlsson and Sorenson Incorporated, 2001.

[42] F. Aymerich, F. Dore, P. Priolo, Prediction of impact-induced delamination in cross-ply composite laminates using cohesive interface elements, Composites Science and Technology 68 (12) (2008) 2383–2390.

[43] M. L. Benzeggagh, M. Kenane, Measurement of mixed-mode delamination fracture toughness of unidirectional glass/epoxy composites with mixed-mode bending apparatus, Composites Science and Technology 56 (4) (1996) 439–449.
[44] NF/F07-101, Essai de choc par simulation de projection de ballast, Association Française de Normalisation, 2002.
[45] ASTM7136/D 7136M-12 standard test method for measuring the damage resistance of a fiber-reinforced polymer matrix composite to a drop-weight impact event, ASTM International. West Conshohocken (PA, USA), 2012.
[46] ASTM7137/D 7137M-12 standard test method for compressive residual strength properties of damaged polymer matrix composite plates, ASTM International. West Conshohocken (PA, USA), 2012.